

Article

# Automated Method for Fractographic Analysis of Shape and Size of Dimples on Fracture Surface of High-Strength Titanium Alloys

Ihor Konovalenko <sup>1</sup>, Pavlo Maruschak <sup>1</sup> and Olegas Prentkovskis <sup>2,\*</sup> 

<sup>1</sup> Department of Industrial Automation, Ternopil National Ivan Pul'uj Technical University, Rus'ka str. 56, 46001 Ternopil, Ukraine; icxxan@gmail.com (I.K.); maruschak.tu.edu@gmail.com (P.M.)

<sup>2</sup> Department of Mobile Machinery and Railway Transport, Faculty of Transport Engineering, Vilnius Gediminas Technical University, Plytinės g. 27, LT-10105 Vilnius, Lithuania

\* Correspondence: olegas.prentkovskis@vgtu.lt; Tel.: +370-5-2744784

Received: 23 January 2018; Accepted: 2 March 2018; Published: 6 March 2018

**Abstract:** An automated method for analyzing the shape and size of dimples of ductile tearing formed during static and impact fracture of titanium alloys VT23 and VT23M is proposed. The method is based on the analysis of the image topology. The method contains the operations of smoothing the initial fractographic image; its convolution with a filter to identify the topological ridges; thresholding with subsequent skeletonization to identify boundaries between dimples; clustering to isolate the connected areas that represent the sought objects—dimples. For each dimple, the following quantitative characteristics were calculated: area, coefficient of roundness and visual depth in units of image intensity. The surface of ductile tearing was studied by analyzing the peculiarities of parameter distribution of the found dimples. The proposed method is applied to fractograms of fracture surfaces of titanium alloys VT23 and VT23M.

**Keywords:** dimples of tearing; fracture mechanisms; image processing; identification of topological ridges; identification of boundaries between dimples; coefficient of roundness; visual depth

## 1. Introduction

It is known that the ductile fracture of materials leads to the formation of dimples of tearing on the fracture surface [1]. Typically, such dimples are formed as a result of the micropore combination in the material during plastic deformation. Dimples are a consequence of the pore rupture and the destruction of the surrounding material [2–4]. A number of models of nucleation, growth, and coalescence of pores are known, but their application under the unpredictable fracture of materials is usually complicated by the need for laboratory determination of many parameters of the material [5–7].

Quantitative fractographic analysis allows for estimating the causes that lead to the formation of dimples of tearing and linking them to the structural parameters of materials, in particular, the size of grains, the shape and number of inclusions. However, this method is time-consuming and requires making many measurements of objects that are located on images of fracture surfaces [8–10]. Interpreting the findings and evaluating the impact of structural and metallurgical factors on the processes of material fracture also requires the accumulation and analysis of large data arrays [10].

The development of algorithms for the automated analysis of images obtained by methods of scanning microscopy allows for a quantitative description of the morphology of material fractures and structures, shapes and sizes of elements on the fracture surface, which increases the accuracy and reliability of the results that were obtained [11,12].

A number of techniques based on the surface image analysis [13–15] have been developed to detect and analyze dimples of tearing on the fracture surface of materials. They use a combination of various

known algorithms for the image analysis (in particular, the analysis of image histograms, thresholds, filtering, wavelets, texture analysis, etc.). Despite their effectiveness, the described algorithms have certain disadvantages.

Quantitative evaluation of the parameters of dimples of ductile tearing located on fractographic images of fractures allows for establishing correlation links between them and the static fracture resistance of structural materials, which is especially important for determining the causes of fracture of materials and structures [16,17].

This is especially important in the case of plastic deformation when strains are initiated and localized, as well as in describing and interpreting the behavior of materials under difficult deformation conditions, in particular, in the dynamic non-equilibrium process (DNP), when a “short-term” exposure of the material structure can completely change its properties. [18]. The use of computer analysis methods to solve such problems allows obtaining fundamentally new information and detailing the physical laws of deformation and fracture of materials, in particular, the micromechanical parameters of pores formed during static and dynamic deformation can be obtained, which are difficult to detect by other methods.

The purpose of this work is to develop and test the method for numerical analysis of the shape and size of dimples of tearing located on the fracture surface of the titanium alloy by analyzing the digital image of the surface.

## 2. Investigation of Static Stretching and Dynamic Non-Equilibrium Process (DNP) of Alloys VT23 and VT23M

The chemical composition of VT23M is the same as that of VT23 (Table 1), however, the range of doping with  $\beta$ -stabilizing alloy elements is 33% less than the corresponding standard for the VT23 alloy. This fact has a significant effect on the improvement of the plastic properties of VT23M compared to VT23 (see Table 2).

**Table 1.** Chemical composition (in %) of titanium alloys VT23 and VT23M.

Fe	Cr	Mo	V	Ti	Al
0.5–0.8	1.0–1.4	1.8–2.5	4.3–5.0	86.0–89.3	4.4–6.3

**Table 2.** Mechanical properties of titanium alloys VT23 and VT23M.

Titanium Alloys	Mechanical Properties		
	$\sigma_{ys}$ , MPa	$\sigma_{us}$ , MPa	$\delta$ , %
VT23	980–1180	1080–1280	15
VT23M	1000–1150	1080–1180	20

Specimens from titanium alloys VT23 and VT23M were used successively to work out loading modes. The specimens were studied under the following schemes of deformation:

- 1 Static stretching to fracture (VT23M and VT23);
- 2 Impact toughness testing (VT22M):
  - in the initial state;
  - after DNP.

Static tests were performed and DNP was realized by impact-oscillatory loading [18,19] on specimens from sheet two-phase high-strength alloy VT23 with a thickness of 3 mm. The breaking force of brittle specimens was in the range of 42–156 kN. The impact toughness was determined on

flat specimens with a thickness of 3 mm, the width of the working area was 10 mm, and the distance between the supports was 60 mm. The depth of the incision was 2 mm.

### 3. Algorithm for Image Analysis

#### 3.1. Algorithm

Fracture of the titanium alloy was considered as a localized deformation process. At the same time, features of its kinetics were reflected on the newly formed surfaces. Consequently, the fracture surface is a complete reflection of the boundary condition of the material, and the peculiarities of its morphology are manifestations of the deformation processes in the material.

In our case, the initial image for the proposed algorithm is a grayscale image of the fracture surface of titanium alloys VT23 and VT23M that was obtained using the scanning electron microscope REM 106-I (JSC "Selmi", Sumy, Ukraine) (Figure 1a,d). The algorithm contains two parts—basic and analytical. The basic part of the algorithm is used to identify areas of the image that belong to dimples of tearing. The analytical part of the algorithm is designed to calculate the quantitative parameters of the found dimples of tearing.

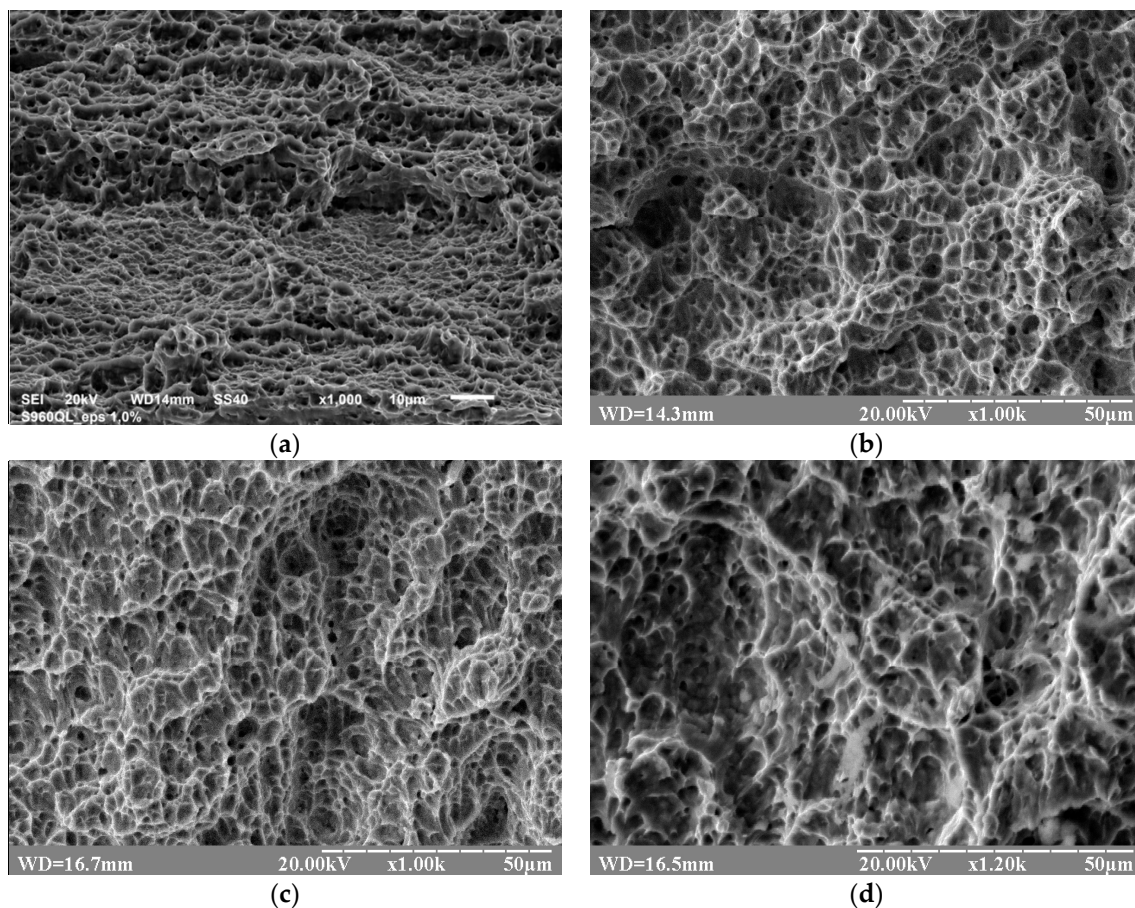


**Figure 1.** SEM images of fracture surfaces of specimens from alloys VT23 (a) and VT23M (b–d) under static (a,b) and impact (c,d) loading.

The fractographic image of the tearing surface of the specimen (Figure 1a–d) can be considered as a surface described by the image intensity distribution function  $i_o(x, y)$ , where  $x = \overline{1}, i_w, y = \overline{1}, i_h$ , and  $i_w, i_h$  are the width and height of the image, respectively. For an 8-bit grayscale image,  $i_o(x, y) \in [0 \dots 255]$ . Topologically, on the surface described by function  $i_o(x, y)$ , dimples of ductile tearing

correspond to “valleys” of the pixel intensity, and the edges of dimples correspond to the “ridges” surrounding them.

A method based on the detection of dimple edges was used to highlight dimples of ductile tearing on the image. For this purpose, intensity differences were calculated for different parts of the image.

Initially, in order to eliminate the ejections of function  $i_o(x, y)$ , it was smoothed by applying the Gaussian filter:

$$i(x, y) = \Gamma[i_o(x, y)], \quad (1)$$

where  $\Gamma$  is the Gaussian operator defined in the neighbourhood of point  $(x, y)$ .

This allows for averaging the intensity of the pixel based on the surrounding area, while giving advantage to the existing value of intensity. Further actions were performed on the filtered image represented by the function  $i(x, y)$ .

Horizontal and vertical gradients of the function  $i(x, y)$  are:

$$G_x(x, y) = \frac{\partial i}{\partial x}, G_y(x, y) = \frac{\partial i}{\partial y}. \quad (2)$$

Low values of the gradient correspond to the ridges and valleys of the function  $i(x, y)$ . To highlight the ridges, the derivatives of the horizontal and vertical gradients were used:

$$L_x = \frac{\partial G_x}{\partial x} = \frac{\partial^2 i}{\partial x^2}, L_y = \frac{\partial G_y}{\partial y} = \frac{\partial^2 i}{\partial y^2}. \quad (3)$$

To evaluate the second derivative at the point  $i(x, y)$ , the Laplace operator was used [20]:

$$L = \nabla^2 i = L_x + L_y = \frac{\partial^2 i}{\partial x^2} + \frac{\partial^2 i}{\partial y^2}. \quad (4)$$

Thus, the edges of dimples (maximums of the function  $i(x, y)$ ) correspond to minimums of  $L$ . To improve the detection of ridges of the function  $i(x, y)$  and to reduce the effect that is caused by local features of the image, partial derivatives (3) were calculated based on pixels with a size  $(2k + 1) \times (2k + 1)$  from a certain neighbourhood. Also, in order to reduce the computational cost, division by the distance between pixels was removed from the calculation of partial derivatives:

$$L_x(x, y) \approx \sum_{n=-k}^k \sum_{m=1}^k i(x - m, y + n) + i(x + m, y + n) - 2i(x, y) \quad (5)$$

$$L_y(x, y) \approx \sum_{n=-k}^k \sum_{m=1}^k i(x + n, y - m) + i(x + n, y + m) - 2i(x, y) \quad (6)$$

In practice, the ridges of the function  $i(x, y)$  were found from expressions (6) by means of convolution the initial image with filters whose kernels are shown in Figure 2a. It is established experimentally that in the case of the investigated images, a good result was obtained from filters with  $k = 3$ . Given this, the white sections of the filter have coefficients of 6 and the black ones have coefficients of 1. In the general case, the coefficient of the white band is  $2k$ . As a result of the described transformations, we obtain an image that is described by the following function:

$$i_L(x, y) = L[i(x, y)]. \quad (7)$$

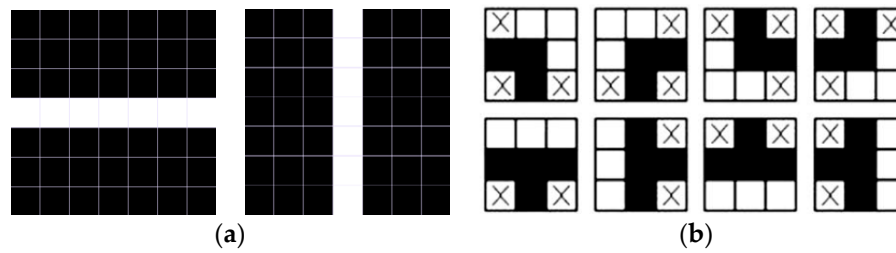


**Figure 2.** Filter kernels to highlight the areas of the image corresponding to the vertex of function  $i(x, y)$  (a); templates for skeletonization (b), mark “x” corresponds to pixels of any color.

Thresholding of image  $i_L$  and skeletonization of the obtained network of edges were performed prior to the segmentation of the edges of dimples. Skeletal image  $i_s$  was obtained by multi-path overlay of templates on the resulting binary image (Figure 2b) [20]. The central black pixel was removed from each area corresponding to one of the templates. Since the edges of dimples should be interconnected, the “hanging” fragments of the skeleton were also removed. Figure 3 shows the initial images (Figure 1) with the well-defined edges of dimples attached to them. As a result of skeletonization, we obtain a set of points that describe the distribution lines between dimples. To expand this boundary, a morphological transformation of dilation with a structural element of  $3 \times 3$  pixels was used to the skeleton.

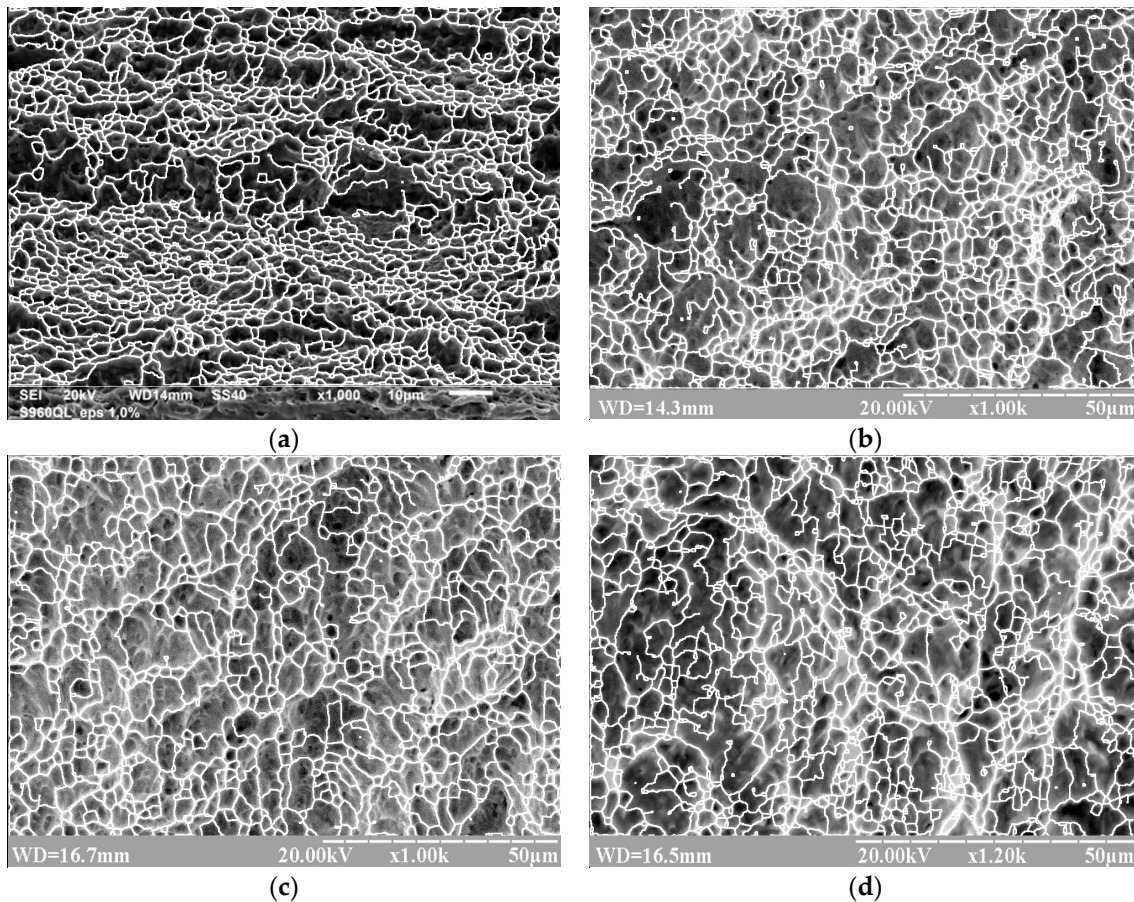


**Figure 3.** The result of recognizing the edges of dimples of ductile tearing on fracture surface of specimens from alloys VT23 (a) and VT23M (b–d) under static (a,b) and impact (c,d) loading.

After that, the connected areas of pixels surrounded by previously found edges were selected. Each of these connected areas represents an individual object—a dimple. Next, the following parameters were calculated for each dimple-object:

- area  $s_i$ ;
- coefficient of roundness  $K_{ci}$ ;
- visual depth  $t_i$  in units of image intensity.

Area  $s_i$  was calculated as the sum of the pixels that are part of the object.

To determine to what degree the shape of dimples approaches the circle, we calculated the coefficient of roundness for each  $i$ -th object.  $K_{ci}$  is the percentage of object pixels that fall in a circle with the same area, whose center is combined with the center of mass of the object [21]:

$$K_{ci} = \frac{\sum_{m=1}^{f_i} g(\vec{r}_m, d_i)}{f_i} \cdot 100\%, \quad g(\vec{r}_m, d_i) = \begin{cases} 1, & \text{when } \left| \vec{r}_m \right| \leq d_i/2 \\ 0, & \text{when } \left| \vec{r}_m \right| > d_i/2 \end{cases} \quad (8)$$

where  $f_i$  is the number of object pixels;  $d_i$  is the diameter of the equivalent circle;  $g(\vec{r}_m, d_i)$  is the indicator function that shows whether the  $m$ -th pixel of the object falls within the boundary of the equivalent circle;  $\vec{r}_m$  is the radius vector directed from the center of the equivalent circle  $C_i(x_{ci}, y_{ci})$  to the  $m$ -th pixel of the object with coordinates  $(x_{cm}, y_{cm})$ . Coordinates of the center of mass of the object:

$$x_{ci} = \sum_{m=1}^{f_i} x_m / f_i, \quad y_{ci} = \sum_{m=1}^{f_i} y_m / f_i. \quad (9)$$

We denote the set of edge pixels of the object by  $BP$  (there is at least one background pixel in their neighbourhood). All of the other pixels of the object will be considered internal. We denote the set of such pixels by  $IP$ . To determine the visual depth of object  $t_i$ , we calculated the mean intensity of the object edge  $i_i^{br}$  and the mean intensity of the dimple-object  $i_i^{dm}$ :

$$i_i^{br} = \sum_{m=1}^{f_i^{bp}} \frac{i_o(x, y)}{f_i^{bp}}, \quad i_o(x, y) \in BP; \quad i_i^{dm} = \sum_{m=1}^{f_i^{ip}} \frac{i_o(x, y)}{f_i^{ip}}, \quad i_o(x, y) \in IP, \quad (10)$$

where  $f_i^{bp}$ ,  $f_i^{ip}$  is the number of elements in the set of  $BP$  and  $IP$ , respectively.

The visual depth of the object in units of image intensity is:

$$t_i = i_i^{br} - i_i^{dm}. \quad (11)$$

For images with different color depth, the relative visual depth is more informative:

$$t_i^r = t_i / i_i^{\max} = (i_i^{br} - i_i^{dm}) / i_i^{\max}, \quad (12)$$

where  $i_i^{\max}$  is the maximum possible value of the pixel intensity for the depth of image  $i_o$ . Very small objects and objects for which the visual depth was very low ( $f_i < f_i^{\min}$ ,  $t_i < t_i^{\min}$ ) were removed from further analysis.

### 3.2. Equivalent Diameters of Dimples Analysis

The investigated fracture surface has an eddy structure that formed as a result of the micropore coalescence and the destruction of interstices between them. The formation of pores was accompanied by localized deformation processes within their boundaries [14,15]. However, they are sufficiently

clear, which allowed for identifying individual dimples and evaluating their parameters. Figure 4a–d shows distribution histograms for equivalent diameters of dimples shown in images from Figure 1.

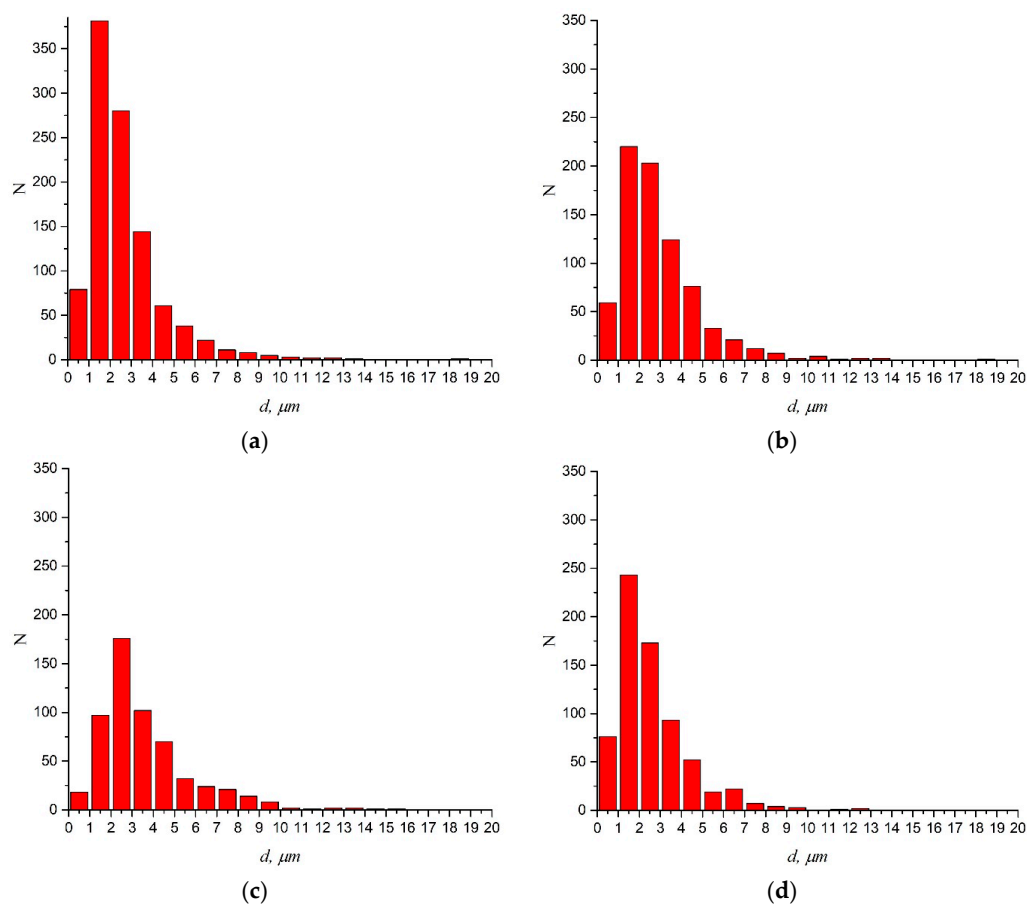


**Figure 4.** Distributions of equivalent diameters  $d_{eqv}$  of dimples for alloys VT23 (a) and VT23M (b–d) under static (a,b) and impact (c,d) loading.

### 3.2.1. Static Stretching

**Alloy VT23.** The maximum array of dimples in this sample  $N_{max} = 381$  pcs is represented by dimples with a size from 1 to 2  $\mu\text{m}$ . The range of the dimples found is from 0.6 to 18.7  $\mu\text{m}$ . That is, the array is formed by relatively large circular dimples with a poorly developed relief at the bottom in the form of mostly light, closed looms. The presence of both large and small dimples in the sample can indicate the heterogeneity of the structure of the material [22].

**Alloy VT23M.** It is found that dimples with a size from 1 to 2  $\mu\text{m}$  formed the largest array  $N_{max} = 220$  pcs. The range of the dimples found was from 0.6 to 18.1  $\mu\text{m}$ . The conglomerates of dimples that were located on the light ridges covered with smaller dimples were found. VT23M is characterized by a reduced range of formed dimples. A reduction in the maximum dimensions of dimples under static deformation and fracture was also noticeable. The obtained results may indicate that a 33% lower range of doping with  $\beta$ -stabilizing elements inherent in this material affects the evolution (accumulation and annihilation rate, mechanisms of origin, and scheme of reconstruction) of the defective substructure and the volume of micropores.

### 3.2.2. Impact Toughness

**Alloy VT23 (without DNP).** It is found that dimples with a size from 2 to 3  $\mu\text{m}$  formed an array  $N_{max} = 176$  pcs. The basic range of the dimples found was from 0.6 to 10  $\mu\text{m}$ . Fracture is characterized

by a fibrous relief, in which the surface is less developed and “smoothed”. Small, shallow, equilibrium dimples were formed in zones with weakened bonds between structural constituents. The interstices between these dimples are formed by a typical ductile mechanism.

Alloy VT23 (with DNP). For this test scheme, it was found that dimples with a size from 1 to 2  $\mu\text{m}$  formed the largest array:  $N_{\text{max}} = 243$  pcs. The range of the dimples found was from 0.6 to 12.3  $\mu\text{m}$ . Morphological analysis of the surface indicates a significant effect of shear processes on the formation of a breakage [23,24]. One can notice a decreased size of dimples compared to static fracture and their greater disorder. The shape of dimples varies from circular to elongated, which is the result of the germination of the main defect and the stochastic process of combining the dimples. The interstices between these sections and the dimples of different shapes are formed by a typical ductile mechanism with the formation of breakouts and deformed sections on the fracture surface. After the DNP realization, the amount of microdefects in the alloy increases, which contributes to the formation of a greater number of micropores, but their sizes are less than those under static deformation. Significant pore densities cause higher energy costs for fracture.

It should be noted that in the process of deformation and fracture, the dimples depend on the structural parameters of the material only partly. This is due to the fact that the local stress-strain state of the material changes at the time of initiation and coalescence of micropores. Since this process is random, we constructed distribution histograms for dimples of tearing in order to illustrate this effect. Note that the main task was not only to determine the size of dimples, but also to evaluate the distribution of their individual groups within the analyzed area for each material examined and type of test.

#### 4. Macroparameters as an Integral Indicator

##### 4.1. Shape and Depth of Dimples

The shape and depth of dimples can be compared (with identical test and image acquisition schemes) with the ductility of the material. It is known that deep conical dimples are inherent in the fracture of very plastic materials. Therefore, it was suggested that an increase in crack resistance is accompanied by an increase in the relative visual depth of dimples and the fracture surface. If we assume that the depth of dimples is proportional to their size, then we can assert that VT23M has better mechanical properties. In addition, VT23M is more plastic at the high rates of deformation and localization of the deformation process. Figure 5 shows distribution histograms of the visual depth of dimples shown in images of Figure 1.

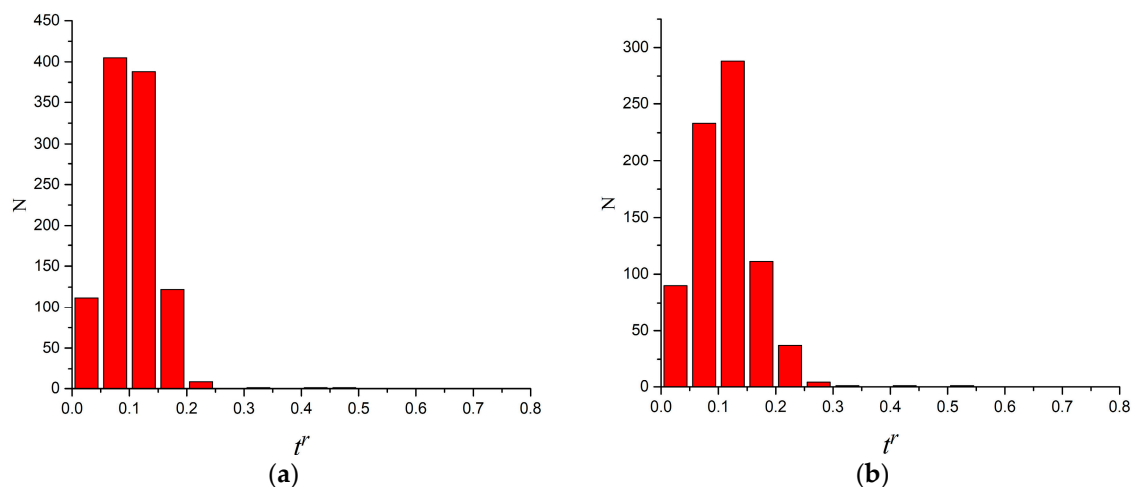
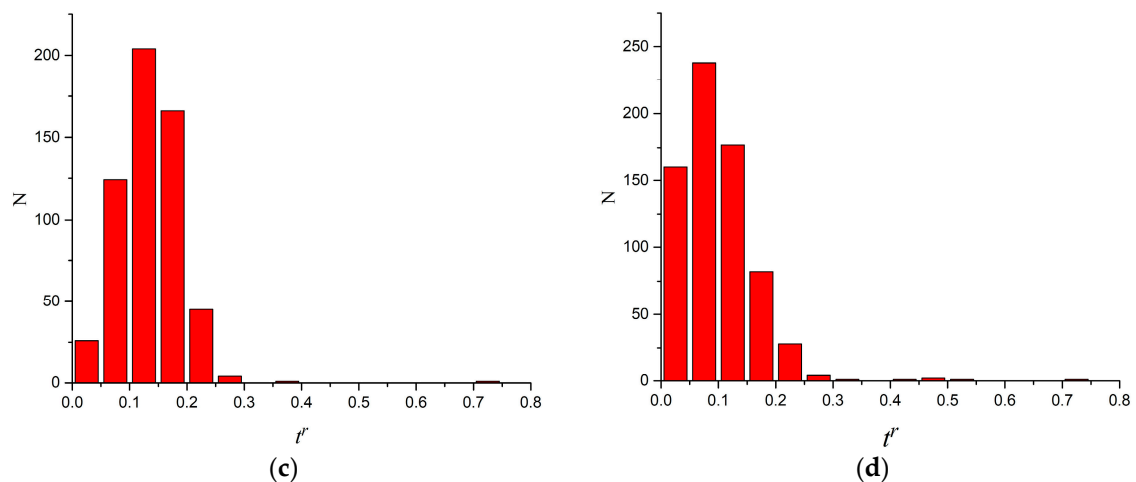


Figure 5. Cont.



**Figure 5.** Histogram of the number of dimples with different levels of relative depth  $t_r^r$  for alloys VT23 (a) and VT23M (b–d) under static (a,b) and impact (c,d) loading.

#### 4.1.1. Static Stretching

*Alloy VT23.* It is shown that the maximum array of dimples  $N_{\max} = 405$  pcs is represented by dimples with  $t_{\max}^r$  from 0.05 to 0.1 in the general range of  $0.02 \leq t_{\max}^r \leq 0.48$ . This indicates similarity in the depth of large and small dimples in the sample.

*Alloy VT23M.* It is established that the maximum array of dimples  $N_{\max} = 288$  pcs is represented by dimples with  $t_{\max}^r$  from 0.1 to 0.15 in the general range of  $0.02 \leq t_{\max}^r \leq 0.82$ . This indicates that these dimples had a shape that was different from the previous ones.

#### 4.1.2. Impact Toughness

*Alloy VT23 (without DNP).* It is established that the maximum array of dimples  $N_{\max} = 204$  pcs is represented by dimples with  $t_{\max}^r$  from 0.1 to 0.15 in the general range of  $0.02 \leq t_{\max}^r \leq 0.73$ .

*Alloy VT23 (with DNP).* It is established that the maximum array of dimples  $N_{\max} = 238$  pcs is represented by dimples with  $t_{\max}^r$  from 0.05 to 0.1 in the general range of  $0.02 \leq t_{\max}^r \leq 0.72$ .

In general, it should be emphasized that the analyzed breakages are formed by small, extremely dispersed dimples, which are separated by regions of relaxation with a micro-dimple structure.

### 4.2. Additional Characteristic of the Surface

#### 4.2.1. Relative Share of the Surface Covered with Dimples and Average Dimple Size

Another characteristic of the surface is the relative share of the surface covered with dimples— $S_r$ . It was calculated as the ratio of the sum of dimple areas to the study area [16]:

$$S_r = S_d/S_o = \sum_{i=0}^N f_i/S_o, \quad (13)$$

where  $S_d = \sum_{i=0}^N f_i$  is the sum of dimple areas in fracture shown in the image;  $N$  is the number of dimples; and,  $S_o$  is the total area of the image.

The average dimple size was also determined, as proposed in [1]:

$$\bar{d} = (S_d/N)^{1/2}, \quad (14)$$

Relative shares of dimples  $S_r$  (%) and interstices ( $S_b$ ), % and other dimple parameters within the analyzed area are given in Table 3.

Table 3. Quantitative results of image analysis.

Schemes of Deformation		Relative Strain, $\varepsilon$ , %	$\bar{d}$ , $\mu\text{m}$	$N$ , pcs	Relative Shares of Dimples, $S_r$ , %	Relative Shares of Interstices, $S_b$ , %
Static fracture	VT23	17.40	2.84	1038	74.04	25.96
	VT23M	22.30	3.13	767	75.19	24.81
Impact fracture	VT23M	-	3.75	571	80.22	19.78
	VT23M after DNP	-	2.74	695	75.59	24.41

The nature of damage to the surface is determined by the parameters of dimples of tearing located on it [3]. It is empirically established that the coefficient of the dimple shape  $K_c$  is informative for their classification. It was believed that the coefficient of roundness  $K_c$  is the localization parameter of the dimple deformation at the microlevel due to the growth of a crack formed as a result of the coalescence of dimples.

Point diagrams showing the dependence of the dimple shape parameter  $K_c$  on its equivalent diameter were constructed (Figure 6). To summarize their results, they were approximated by a straight line using the least squares method. It is found that straight lines were located at angles  $80^\circ$ ,  $81^\circ$ ,  $79^\circ$ ,  $77^\circ$  to the vertical line, respectively, i.e., in a sufficiently narrow range. At the same time, an increase in the angle of inclination indicates an increase in the integral approximation of the analyzed dimples to the circular shape. It is found that small dimples of tearing are close to the circular shape (Figure 6). Further propagation and coalescence of dimples indicates a certain tendency to acquire a more circular shape. In addition, boundary effects become smooth and get orientation along a certain direction.

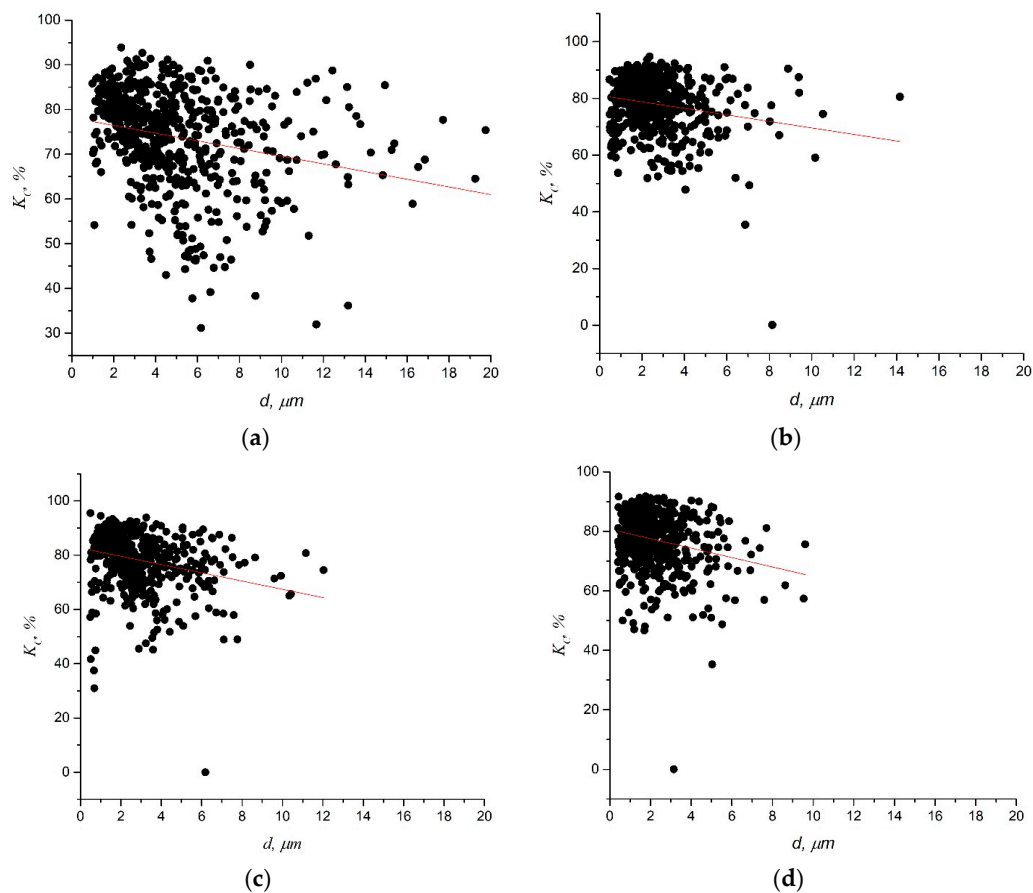


Figure 6. Dependence of the dimple shape parameter  $K_c$  on its equivalent diameter  $d$  for alloys VT23 (a) and VT23M (b–d) under static (a,b) and impact (c,d) loading.

#### 4.2.2. Static Stretching

It was found that titanium alloy VT23M has dimples of a somewhat rounder shape than alloy VT23. This is due to certain features of the technological process of obtaining the material and the course of the damage accumulation process. The circular dimples of tearing were formed on areas of structural heterogeneity, in particular, in the vicinity of inclusions and on boundaries between grains, which was accompanied by the accumulation of local strains and the fracture of the material. The consolidation of dimples is primarily due to the transition to a volumetric stressed state, which causes the growth and coalescence of defects with the formation of large dimples [25–27].

#### 4.2.3. Impact Toughness

Alloy VT23M (with and without DNP). For both cases of impact fracture of the material, it was found that dimples have a more brittle appearance. However, the influence of the plastic flow of the material is noticeable. The deformed contours of dimples with sharp edges and their deformation in the direction of fracture process indicate a mixed (ductile-brittle) mechanism of the formation of the investigated surface.

### 5. Conclusions

A method is proposed for the analysis of ductile separation surfaces of high-strength titanium alloys VT23 and VT23M that is based on their fractograms obtained using an electronic scanning microscope. The method is implemented using the algorithm for detecting the edges of dimples of tearing, which contains operations of smoothing the initial image; its convolution with a filter to detect edges; thresholding with subsequent skeletonization to identify boundaries between dimples; clustering to allocate connected areas; and, calculating the quantitative indicators of the found objects.

The feature of the objects detected by this method is that they are surrounded by distribution ridges of intensity on the original image. The proposed method takes into account this feature and is oriented on its search, which allows for a more precise identification of edges of such objects, in contrast to the methods that focused on the direct analysis of the image pixel intensity.

Based on the analysis of fractographic images, the regularities in static and dynamic fracture of high-strength titanium alloys have been established, and quantitative evaluation of the parameters of their fracture surface was performed. It was found that the fracture surface of specimens in both test types is formed by the dimple mechanism. The size of dimples was from 0.5  $\mu\text{m}$  to 20.0  $\mu\text{m}$ . The distribution diagrams of dimple sizes for each alloy, including the type of loading, have been constructed.

It was found that titanium alloy VT23M had better deformation properties at macro and micro levels than VT23. This is confirmed by a higher relative parameter of dimples of tearing  $\bar{d} = 3.13 \mu\text{m}$  (VT23M) and 2.84  $\mu\text{m}$  (VT23). DNP causes a decrease in the size of dimples of tearing and an increase in their number when compared with the initial state of alloy VT23M in impact strength testing.

**Author Contributions:** Pavlo Maruschak and Olegas Prentkovskis conceived and designed the experiments; Ihor Konovalenko performed the experiments and analyzed the micro pictures; Pavlo Maruschak, Ihor Konovalenko and Olegas Prentkovskis wrote the paper.

**Conflicts of Interest:** The authors declare no conflict of interest.

### References

1. Broek, D. The role of inclusions in ductile fracture and fracture toughness. *Eng. Fract. Mech.* **1973**, *5*, 57–66. [[CrossRef](#)]
2. Garrison, W.M., Jr.; Wojcieszynski, A.L. A discussion of the spacing of inclusions in the volume and of the spacing of inclusion nucleated voids on fracture surfaces of steels. *Mater. Sci. Eng. A* **2009**, *505*, 52–61. [[CrossRef](#)]

3. Srivastava, A.; Ponson, L.; Osovski, S.; Bouchaud, E.; Tvergaard, V.; Needleman, A. Effect of inclusion density on ductile fracture toughness and roughness. *J. Mech. Phys. Solids* **2014**, *63*, 62–79. [[CrossRef](#)]
4. Osovski, S.; Srivastava, A.; Ponson, L.; Bouchaud, E.; Tvergaard, V.; Ravi-Chandar, K.; Needleman, A. The effect of loading rate on ductile fracture toughness and fracture surface roughness. *J. Mech. Phys. Solids* **2015**, *76*, 20–46. [[CrossRef](#)]
5. Kim, J.; Gao, X.; Srivatsan, T.S. Modeling of void growth in ductile solids: Effects of stress triaxiality and initial porosity. *Eng. Fract. Mech.* **2004**, *71*, 379–400. [[CrossRef](#)]
6. Kruglova, A.; Roland, M.; Diebels, S.; Dahmen, T.; Slusallek, P.; Mücklich, F. Modelling and characterization of ductile fracture surface in Al-Si alloys by means of Voronoi tessellation. *Mater. Charact.* **2017**, *131*, 1–11. [[CrossRef](#)]
7. Osovski, S.; Srivastava, A.; Williams, J.C.; Needleman, A. Grain boundary crack growth in meta-stable titanium beta alloys. *Acta Mater.* **2015**, *82*, 167–178. [[CrossRef](#)]
8. Underwood, E. Quantitative fractography. In *Applied Metallography*; Voort, G.V., Ed.; Springer: Berlin, Germany, 1986; pp. 101–122.
9. Li, X.; Tian, J.; Kang, Y.; Wang, Z. Quantitative analysis of fracture surface by roughness and fractal method. *Scr. Metall. Mater.* **1995**, *33*, 803–809. [[CrossRef](#)]
10. Kosarevych, R.Y.; Student, O.Z.; Svirs'ka, L.M.; Rusyn, B.P.; Nykyforchyn, H.M. Computer analysis of characteristic elements of fractographic images. *Mat. Sci.* **2013**, *48*, 474–481. [[CrossRef](#)]
11. Gonzalez, R.C.; Woods, R.E. *Digital Image Processing*, 3rd ed.; Pearson Education: London, UK, 2008.
12. Maruschak, P.; Konovalenko, I.; Prentkovskis, O.; Tsyrunlyk, O. Digital analysis of shape and size of dimples of ductile tearing on fracture surface of long-operated steel. *Procedia Eng.* **2016**, *134*, 437–442. [[CrossRef](#)]
13. Dutta, S.; Das, A.; Barat, K.; Roy, H. Automatic characterization of fracture surfaces of AISI 304LN stainless steel using image texture analysis. *Measurement* **2012**, *45*, 1140–1150. [[CrossRef](#)]
14. Bastidas-Rodriguez, M.X.; Prieto-Ortiz, F.A.; Espejo, E. Fractographic classification in metallic materials by using computer vision. *Eng. Fail. Anal.* **2016**, *59*, 237–252. [[CrossRef](#)]
15. Kosarevych, R.J.; Rusyn, B.P.; Korniy, V.V.; Kerod, T.I. Image segmentation based on the evaluation of the tendency of image elements to form clusters with the help of point field characteristics. *Cybern. Syst. Anal.* **2015**, *51*, 704–713. [[CrossRef](#)]
16. Kudrya, A.V.; Sokolovskaya, E.A.; Trachenko, V.A.; Le Hai, N.; Skorodumov, S.V.; Papina, K.B. Measurement of nonuniformity of fracture in structural steels with heterogeneous structure. *Met. Sci. Heat Treat.* **2015**, *57*, 190–196. [[CrossRef](#)]
17. Maruschak, P.; Konovalenko, I.; Prentkovskis, O.; Chausov, M.; Pylypenko, A. Methods and some results of automated analysis of ductile failure mechanisms of titanium alloy VT-22. *Procedia Eng.* **2016**, *134*, 475–480. [[CrossRef](#)]
18. Chausov, M.G.; Maruschak, P.O.; Hutsaylyuk, V.; Śnieżek, L.; Pylypenko, A.P. Effect of complex combined loading mode on the fracture toughness of titanium alloys. *Vacuum* **2018**, *147*, 51–57. [[CrossRef](#)]
19. Chausov, M.G.; Maruschak, P.O.; Pylypenko, A.P.; Berezin, V.B.; Prentkovskis, O. Structural self-organization of titanium alloys under impulse force action. *Mater. Test.* **2017**, *59*, 567–569. [[CrossRef](#)]
20. Marushchak, P.O.; Konovalenko, I.V. Computer evaluation of the depth of thermomechanical fatigue cracks according to their length. *Mater. Sci.* **2012**, *48*, 54–64. [[CrossRef](#)]
21. Konovalenko, I.V.; Marushchak, P.O.; Bishchak, R.T. Automated estimation of damage to the surface of gas main by corrosion pittings. *Mater. Sci.* **2014**, *49*, 493–500. [[CrossRef](#)]
22. Ohashi, M. Extreme value analysis of ductile fracture surface by dimpled rupture associated with fracture behavior of tensile specimens. *J. Mater. Sci.* **2007**, *42*, 9877–9887. [[CrossRef](#)]
23. Maruschak, P.; Menou, A.; Chausov, M.; Mocharskyi, V. Fractographic analysis of surface and failure mechanisms of nanotitanium after laser shock-wave treatment. *Key Eng. Mater.* **2014**, *592–593*, 346–349. [[CrossRef](#)]
24. Rittel, D.; Osovski, S. Dynamic failure by adiabatic shear banding. *Int. J. Fract.* **2010**, *162*, 177–185. [[CrossRef](#)]
25. Yasniy, P.; Maruschak, P.; Bishchak, R.; Hlado, V.; Pylypenko, A. Damage and fracture of heat resistance steel under cyclic thermal loading. *Theor. Appl. Fract. Mech.* **2009**, *52*, 22–25. [[CrossRef](#)]

26. Faleskog, J.; Gao, X.; Shih, C.F. Cell model for nonlinear fracture analysis—I. Micromechanics calibration. *Int. J. Fract.* **1998**, *89*, 355–373. [[CrossRef](#)]
27. Romanova, V.; Balokhonov, R.; Panin, A.; Kazachenok, M.; Kozelskaya, A. Micro-and mesomechanical aspects of deformation-induced surface roughening in polycrystalline titanium. *Mater. Sci. Eng. A.* **2017**, *697*, 248–258. [[CrossRef](#)]



© 2018 by the authors. Licensee MDPI, Basel, Switzerland. This article is an open access article distributed under the terms and conditions of the Creative Commons Attribution (CC BY) license (<http://creativecommons.org/licenses/by/4.0/>).